ACDIS

Research Report

Non-anthropogenic Influences on Global Average Temperature

Chenghao Ding
Department of Nuclear, Plasma, and Radiological Engineering
University of Illinois at Urbana-Champaign

Clifford E. Singer
Program in Arms Control & Domestic and International Security
University of Illinois at Urbana-Champaign

Research of the Program in Arms Control
& Domestic and International Security

University of Illinois at Urbana–Champaign

July 2022

The research for this publication is supported by the University of Illinois. It is produced by the Program in Arms Control & Domestic and International Security at the University of Illinois at Urbana-Champaign.

ACDIS Publication Series: The ACDIS *Occasional Paper* series is designed for circulating the scholarly analytical results of faculty, students, and visiting researchers associated with ACDIS. The ACDIS *Research Reports* series publishes technical reports and findings from security related research. The ACDIS *Commentary* series serves to inform U.S. and international policy decisions. The ACDIS *International Security Policy Brief* series contains previous works with a purpose similar to those in the *Commentary* series. ACDIS *Swords and Ploughshares* contains archives of a periodic journal of collected articles aimed at a general audience. For additional information and to download publications, visit the ACDIS home page at: http://acdis.illinois.edu/

Published 2022 by ACDIS//ACDIS DIN:3.2022

University of Illinois at Urbana–Champaign 359 Armory Building, 505 E. Armory Ave.
Champaign, IL 61820-6237

Series Editor: Jazmin Tejeda

Non-anthropogenic Influences on Global Average Temperature

CHENGHAO DING
Department of Nuclear, Plasma, and Radiological Engineering
University of Illinois at Urbana Champaign

CLIFFORD E. SINGER
csinger@illinois.edu
Program in Arms Control & Domestic and International Security
University of Illinois at Urbana Champaign

Non-anthropogenic influences on global average temperature are divided into short-term transients and slower evolution of trends in radiative forcing. Short-term variations include Schwabe cycle solar irradiance oscillations with a period of c. 11 yrs, radiative shielding from large volcanic eruptions, and variations in global average temperature correlated with the El Niño Southern Oscillation (ENSO). The analysis described here examines deviations of total solar irradiance from slower evolutionary trends, of large departures of stratospheric aerosol optical depth (AOD) from a temporal average, and of a multivariate ENSO index (MEI) around a temporal average. These are correlated with short-term variations of global average temperature. Comparison with estimates of global average temperature in the twentieth century show dips following two of the three largest volcanic AOD excursions. Those are from the 1991 Pinatubo and 1963 Gunung Agung eruptions. However, the 1983 maximum calendar year cooling following the 1982 El Chinchón eruption overlapped with the 1983 largest positive ENSO associated calendar year global warming in the twentieth century. These comparisons suggest subtracting transient effects from global average temperature before using the result to calibrate a reduced complexity model of the impact of slower evolution of radiative forcing.

1. Rationale

This is the third in a series of reports describing components of a revision an earlier form [1] of the Climate Action Gaming Experiment (CAGE) model. One use of CAGE is to conduct controlled experiments on how people respond to information about the physical and economic consequences of different possible future evolutions of radiative forcing and atmospheric carbon dioxide concentrations. From this point of view, *Homo sapiens* is one of many species that are part of an overall biological feedback complex responding to climate change. While small scale controlled experiments with other species look at different feedback mechanisms, like open air exposure of *Zea mays* field corn to elevated CO_2 levels, here *Homo sapiens* is also viewed as one component of the biospheric response to climate change. It is for this reason that the topic of the present report is described as non-anthropogenic influences. This is instead of using the term natural [2], to avoid an implicit suggestion that the human part of the biospheric response is somehow outside the realm of a comprehensive experimentally informed analysis of the feedback system.

A division of non-anthropogenic influences on global average temperature into slowly evolving and more transient variations is motivated by differences in timescales. The Schwabe sunspot cycle has an increase in radiative forcing for about 5.5 years, following by decrease for about the next 5.5 years. The time between the maximum temporary increases in global average temperature associated with the ENSO cycle averages between 3 to 5 years [3]. Increases in atmospheric optical depth after large volcanic eruptions in the twentieth century have declined back to background fluctuation levels after at most about 3 years. By way of contrast, the cosine fit to the Gleissberg cycle [4] for slower evolution of solar irradiance discussed below has a period of 87.5 years. That is comparable to the timescale for evolution of anthropogenic increases in radiative forcing, which had about half a century growth rate timescale during an approximately exponential growth period. For such comparatively slow changes, added thermal energy has had time to transport hundreds

of meters deep into the ocean [5]. While approximately exponential growth in radiative forcing continued for decades, thermal energy transport into the deeper ocean limited surface temperature increase that would have otherwise led to larger radiative losses and lower overall thermal energy uptake. Transient changes on timescales too short to allow for as much associated thermal energy exchange between the surface and deeper ocean can be expected to lead to compensating changes in radiative energy transport that produce comparatively less change in overall thermal energy change per unit change in radiative forcing. Thus, it is not appropriate to use a simple global heat balance model of the form

$$c_{th}\tau' = F - \tau/\beta \tag{1.1}$$

for both short-term transients and evolution of radiative forcing on a multi-decadal timescale.

The approach to transients used here is similar to that of Foster and Rahmstorf [6], which updated similar work by Lean and Rind [7]. Starting with Goddard Institute for Space Science estimates of global average temperature [8], Foster and Rahmstorf give estimates of the ratios of global average temperature impact to three different independent data streams. In each case, the temperature impact lags by a different number of months behind the data stream numbers. Table 1 lists those lags and low ("2 σ"), middle, and high ("2 σ") estimate of those ratios.

Table 1. Month Lags and Ratios for °C Impacts Transients

Type	Lag (Months)	Low	Medium	High
Total Solar Irradiance	1	0.009	0.084	0.157
Atmospheric Optical Depth	7	-1.43	-2.36	-3.31
Multivariate ENSO Index	4	0.050	0.080	0.109

A difference here from what was done by Foster and Rahmstorf is that analysis of such transients here includes times that go back before 1950. As described in more detail in the Appendix A below, that required a different approach to the Schwabe sunspot cycle. It also required combining different data sources for the multivariate ENSO index and for atmospheric optical depth. In each case, however, estimated historical effects on globally and annually averaged temperature were proportional to an independently measured quantity, after accounting for temporal lag between that quantity and changes in global average temperature.

What are plotted in Figures 1b, 2a, and 2b are results for the medium values of the coefficients listed in Table 1. However, the estimated upper and lower limits for the coefficients for impacts of transients on global average temperature listed in Table 1 cover a substantial range, particularly for the case of total solar irradiance. Thus, for subsequent applications the temperature impacts shown in Figures 1b and 2a will be multiplied by adjustable coefficients to be estimated along with the other parameters in the global heat balance equation (1.1).

2. Total Solar Irradiance and Radiative Forcing

For the Goddard Institute for Space Studies (GISS) global average temperature estimates [8], figure 3 from Foster and Rahmstorf gives an estimate of $0.084°/(\mathrm{W/m^2}$ of TSI) where TSI is the difference in total solar irradiance from a linear fit to the evolution of TSI. As illustrated here in Figure 1a, such a linear fit looks appropriate for the 1979–2011 span used by Foster and Rahmstorf, but not for a time span including more of the twentieth century.

The smooth curve shown in Figure 1a is a least squares fit of the difference between TSI and the average TSI for 1745 through 1755. That average is chosen because 1750 was a Schwabe

cycle peak year. Other estimates of radiative forcing used in this report series are differences from radiative forcing in 1750. The parameter τ in equation (1.1) is operationally defined here as the difference between global average temperature and the temperature that would be in equilibrium with a constant radiative forcing equal to that in 1750. (Since TSI was not constant around 1750, the average over one Scwhabe cycle was used instead of the value in 1750.) The smooth curve in Figure 1a uses a sum of three cosine oscillations and a constant. The parameters of that curve are listed in Table 2.

TSI is incident solar radiation on the area projected onto a plane perpendicular to a line to the sun at a distance of one astronomical unit. The ratio 0.1278 in Table 1 of radiative forcing to total solar irradiance is $0.25 \times (1 - 0.29) \times 0.72$. The factor 0.25 is the ratio of the area of a circle with to the area of a sphere with the same radius. The factor (1-0.29) is a correction for effective average albedo, and the factor 0.72 accounts for the spectral dependence of effective radiative forcing, per Section 7.3.4.4 of [2]. The smooth curve in Figure 1a is thus multiplied by a factor 0.1278 for the purpose of adding solar radiative forcing to other components of radiative forcing. The method used to define the parameters in Table 2 is described in Appendix A.

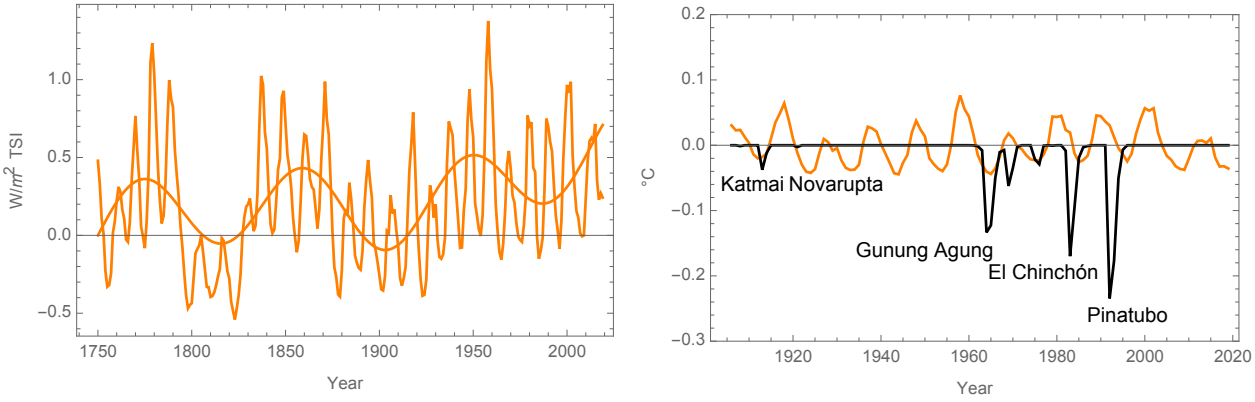

Figure 1. (a) Constant plus three cosine fit and data for annually averaged difference between total solar irradiance and its year 1745–1755 average. (b) Positive and negative globally and annually averaged temperature transients from the Schwabe cycle, and negative transients from large volcanic eruptions.

Table 2. Slow Variations $b_1 \cos(2\pi(t - b_2)/b_3)$ of Solar Radiative Forcing

Type	b_1(W/m^2)	b_2 (Julian Year)	b_3 (Years)
Grand Minimum	-0.046	1650	842
Gleissberg	0.032	1772	87.5
Triple Gleissberg	-0.020	1927	270
Additional Constant	0.023	Forcing/TSI:	0.1278

Figure 1b shows the Schwabe cycle globally and annually averaged global average temperature impacts computed using the 0.084°C/(W/m^2 TSI) ratio listed in Table 1. The TSI used for this is the difference between the jagged and smooth curves shown in Figure 1a. Also shown in Figure 1b are estimated impacts from three large volcanic eruptions and additional smaller ones, as described in the next section.

3. Volcanoes and ENSO

Radiative forcing from volcanoes is divided into large transients and a low-level background. The low-level background is all of the AOD up through 0.012. That threshold limit is chosen to be twice the average of the low-level background from 1906–2012 rounded to the nearest 0.001. All with AOD>0.012 are designated as transient. Multiplying the transient AOD by the factor -2.36°C/AOD listed in Table 1, lagging by 7 months, and taking the annual averages gives the negative curves plotted in Figures 1b, 2a, and 2b. For this purpose there are three cases, all before 1950, that are for volcanic eruptions that are extratropical, i.e. located more than 20 degrees of latitude from the equator. Of those three cases, only the 1912 Katmai Novarupta eruption in Alaska produced a calculated change of magnitude more than 0.003°C. Details on why [9] and how a factor somewhat less than 1 multiplies the -2.36°C/AOD ratio for extratropical volcanoes are described in Appendix A.

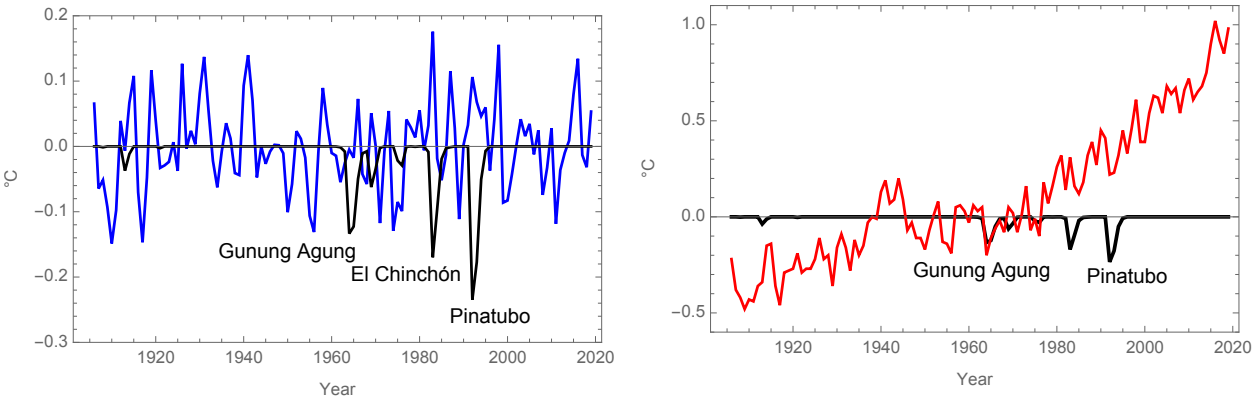

Figure 2. (a) Globally and annually averaged temperature changes correlated with ENSO variations, compared to cooling from large volcanic eruptions. (b) Differences between globally and annually averaged temperature and its 1951–1980 average, compared to cooling from large volcanic eruptions.

Figure 2a shows the annually averaged four-month lagged product of the MEI index and the 0.080°C/MEI factor listed in Table 1. The 1983 peak annually averaged cooling of following the El Chinchón eruption and the largest twentieth century annual ENSO-associate warming in the same year nearly cancel. The calculated sum of volcanic, ENSO-related, and Schwabe cycle transients for 1983 is $-0.17 + 0.18 + 0.02 = 0.03$°C. By 1984, there is less calculated volcanic cooling, but the ENSO-related transient has changed to slightly negative. The corresponding sum for 1984 is $-0.10 - 0.02 - 0.01 = -0.13$°C. A consistent coincidence between volcanic cooling and dips in the annually and globally average temperature plotted in Figure 2b is thus clearer in the two years following the 1963 Gugung Agung and 1981 Pinatubo eruptions. These results illustrate why it was considered useful to be able to subtract transient effects from the global average temperature in preparation for calibrating parameters in the global heat balance equation against historical data.

Appendix A. Data and Methods

A.1. **TSI Time Series.** Estimates of annually averaged total solar irradiance from 1610–2018 came from the Laboratory for Atmospheric and Space Physics Interactive Solar Irradiance Data Center (LISIRD) [10, 11, 12, 13]. For 2019, the difference between the averages of non-zero daily satellite measurements of TSI [14, 15, 16] for 2019 and 2018 was added to the 2018 LISIRD number.

A.2. **AOD Time Series.** Monthly estimates of stratospheric aerosol optical depth [17] for 1850 through September of 2012 were obtained from the NASA Goddard Institute for Space Studies [18]. This contained all of the data needed to produce the volcanic cooling results shown above. As noted above, that is for AOD values in excess of a threshold, set at 0.012 to make it twice the 1906–2012 average of the below-threshold AOD values of 0.00592, rounded to 0.006 because the GISS data had three significant figures.

The threshold limit computed using 1906–2012 GISS AOD numbers was the same as that obtained from the June 1905–May 2019 AOD range that was used to check that no over threshold volcanic eruptions produced a computed annually averaged global cooling after 1995. (For this purpose, to extend AOD estimates through May of 2019, monthly estimates for 2001–2018 were found from Carn et al. [19] and for 2018 through May of 2019 from Kloss et al. [20].) The 2001–2012 average from Carn et al. was higher by 0.0294 than that average for GISS. That number was subtracted from the 2013–2018 Carn et al. numbers, and the result was rounded to the nearest 0.001, and then that result was appended to the GISS numbers. For January–May of 2019, the Kloss et al. AOD, which was measured at a different wavelength, was multiplied by the year 2018 ratio 0.556 of the shifted Carn et al. numbers to the year 2018 Kloss et al. numbers to extend the AOD estimates. (The resulting average of below-threshold AOD was 0.00587, which also rounds to the 0.006 value of half of the AOD threshold used.) The variation of below-threshold AOD by ± 0.006 around a pre-industrial average, and of associated radiative forcing and global average temperature impact, is approximated for CAGE as a minor component of substantially larger random departures of globally and annually averaged temperature from an underlying trend. So, no additional transients from below-threshold variations in AOD are computed herein.

A.3. **MEI Time Series.** One time series used for the Multivariate ENSO Index included the September 1905–August 2004 part of a 1871–2005 monthly time series [21, 22]. The other included the September 2004–August 2019 part of 1979–November 2021 series [23]. The 1871 series has zero mean and unit standard deviation. The 1979–2021 series is updated monthly and thus would not be backward compatible if it were continually readjusted to have zero mean and unit standard deviation. Linear transformations of September 1905–August 1949 and September 1949–August 2004 parts of the first above-mentioned MEI time series, and of the September 2004–August 2019 part of the second MEI time series, converted all three to have zero mean and unit standard deviation. Each of the three results and any combination thereof thus had zero mean. The standard deviations of both the entire time series (September 1905–August 2019) and the last two (September 1949–August 2019) were 0.999. This approach was in preparation for comparing calibration of parameters in the global heat balance equation against different spans of historical data.

A.4. **Solar Forcing Fit.** The method used to define the parameters in Table 1 is as follows. Fit the 1610–2019 amplitude of a Grand solar cycle with a minimum in the middle year 1650 of the Maunder minimum and a period of 842 years from the average of 710 and 975 year peaks in isotope-derived solar power spectra [24]. Then add a constant plus cosine term to start a least squares fit starting from an 88 year estimate of the Gleissberg period using residuals from the 1750-2019 part of the Grand solar cycle fit. Fit the residuals from that fit with another constant plus cosine term, starting the search with a 285 year period in the 282–292 range of intermediate periods for a years 4700-3500 before 1950 data stream not including a grand minimum, as described in McCracken et al. [24]. The third cosine function is included to avoid the fit having a rising trend from 1905–2019. Including the constant term in Table 2 ensures that this fit to solar radiative forcing is zero in 1750.

A.5. **Extratropical Volcanoes.** Marshall et al. [9] compared differences in effective radiative forcing (ERF) response in simulations of 41 pairs volcanic eruptions with different volumes of SO_2 emissions and locations for eruptions. For each level of SO_2 emission and location, simulations were

done for eruptions at the beginning of the first full month of winter and of the first full month of summer. They divided the locations into tropical (within 20 degrees latitude of the equator) and extratropical. They found that the time it takes for spread of stratospheric haze from extratropical winter eruptions leads to more change in ERF in the summer in the hemisphere of eruption, compared to less change in ERF in that hemisphere for summer eruptions in that hemisphere.

The maximum of a set of random SO_2 emissions volumes in the study by Marshall et al. was much larger than the maximum twentieth century value. So, their supplementary material was used for a re-analysis of the 13 pairs of cases with SO_2 emissions less than 38 million metric tons (a limit chosen to be approximately twice that of Mount Pinatubo emission of about 20 million metric tonnes of SO_2 [19]). The AOD for this set of cases was small enough that ratios of ERF to AOD were fit for simplicity as a function of AOD, rather than as a function of 1+Exp(-AOD) as in Marshall et al. The result was that there was more annually averaged ERF change for tropical than extratropical eruptions, averaged over the twelve months following the eruption. The change for winter eruptions was larger than for summer eruptions. The ratio of ERF from extratropical summer and winter eruptions to the ERF from tropical eruptions was fit with the function

$$r = 0.86 + 0.10\cos(2\pi f) \tag{A.1}$$

Here f is the fraction of a year between the first day of the first full month of winter and the time of the eruption.

The monthly AOD values for extratropical eruptions for the first twelve months, including the month of eruption, were multiplied by the factor r. That difference between ERF/AOD ratios for extratropical and tropical eruptions averaged over the second year after eruption is 0.1 times that for the first year, and so was not accounted for. The third year AOD for the twentieth century extratropical eruptions was below the above-mentioned threshold level, so a correction factor similar to r for third year after eruption was not needed.

The correction described here for difference between effects on global average temperature between tropical and extratropical volcanoes has a very small impact for twentieth century volcanoes. It is accounted for here primarily as a reminder that globally averaged atmospheric optical depth estimates are not necessarily by themselves always sufficient to estimate transient impacts on global average temperature.

References

[1] Singer, C. and L. Matchett, 2015. Climate action gaming experiment: Methods and example results, *Challenges* **6**, 202–228, doi:10.3390/challe6020202.

[2] IPCC, 2021. *Climate Change 2021: The Physical Science Basis. Contribution of Working Group I to the Sixth Assessment Report of the Intergovernmental Panel on Climate Change*, V. Masson-Delmotte, P. Zhai, A. Pirani, S. L. Connors, C. Pèan, S. Berger, N. Caud, Y. Chen, L. Goldfarb, M. I. Gomis, M. Huang, K. Leitzell, E. Lonnoy, J. B. R. Matthews, T. K. Maycock, T. Waterfield, O. Yelekçi, R. Yu and B. Zhou (eds.). Cambridge University Press. In Press, https://www.ipcc.ch/report/sixth-assessment-report-working-group-i/.

[3] Climate Prediction Center Internet Team. 2005. El Niño and La Niña ocean temperature patterns. NOAA National Weather Service, December 19, https://www.cpc.ncep.noaa.gov/products/analysis_monitoring/ensocycle/ensocycle.shtml.

[4] Peristykh, A. N., and P. E. Damon. 2003. Persistence of the Gleissberg 88-year solar cycle over the last ∼12,000 years: Evidence from cosmogenic isotopes. *Journal of Geophysical Research Space Physics* **108**, SSH1-1 to SSH1-15, https://doi.org/10.1029/2002JA009390.

[5] Cheng, L., K. Trenberth, J. Fasullo, T. Boyer, J. Abraham, and J. Zhu. 2017. Improved estimates of ocean heat content from 1960 to 2015, *Science Advances* **3**, e1601545, 10 March, https:/doi:10.1126.1601545.

[6] Foster, G., and S. Rahmstorf. 2011. Global temperature evolution 1979–2010, *Environmental Research Letters* **6**, 044022, https://doi.org/10.1088/1748-9326/6/4/044022.

[7] Lean, J., and D. H. Rind. 2009. How natural and anthropogenic influences alter global and regional surface temperatures: 1889 to 2006, *Geophysics Research Letters* **35**, L18701, https://doi.org/10.1029/2008GL034864.

[8] GISTEMP Team. 2021. *GISS Surface Temperature Analysis (GISTEMP), version 4.* NASA Goddard Institute for Space Studies, https://data.giss.nasa.gov/gistemp/; https://data.giss.nasa.gov/gistemp/tabledata_v4/GLB.Ts+dSST.csv, accessed December 22, 2021.

[9] Marshall, L. R., C. J. Smith, P. M. Forster, T. Aubry, T. Andrews, and A. Schmidt. 2020. Large variations in volcanic aerosol forcing efficiency due to eruption source parameters and rapid adjustments, *Geophysical Research Letters* **47**, e2020GL090241, https://doi.org/10.1029/2020GL090241.

[10] Kopp, G., N, Krivova, J. Lean, and C. J. Wu. 2019. The impact of the revised sunspot record on solar irradiance reconstructions. *Solar Physics* **291**, 2951–2956, https://doi.org/10.1007/s11207-016-0853-x.

[11] LASP Interactive Solar Irradiance Data Center. 2021. Historical total solar irradiance reconstruction, time series, https://lasp.colorado.edu/lisird/data/historical_tsi, accessed September 15, 2021.

[12] LASP Interactive Solar Irradiance Datacenter. 2021. Historical total solar irradiance reconstruction, time series. https://lasp.colorado.edu/lisird/latis/dap/historical_tsi.csv?&time%3E=1610-01-01T00:00:00.000Z&time%3C=2021-09-07T23:10:00.000Z, accessed December 18, 2021.

[13] Dudok de Wit, T., G. Kopp, C. Fröhlich, and M. Schöll. 2017. Methodology to create a new Total Solar Irradiance record: Making a composite out of multiple data records, *Geophysical Research Letters*, https://doi.org/10.1002/2016GL071866.

[14] Wu, C.-J., N. A. Krivova, S. K. Solanki, and I. G. Usoskin. 2018. Solar total and spectral irradiance reconstruction over the last 9000 years. *Astronomy and Astrophysics* **620**, A120. https://doi.org/10.1051/0004-6361/201832956.

[15] SORCE. 2020. Total Solar Irradiance, Solar radiation and climate experiment, University of Colorado, Boulder, Laboratory for Atmospheric and Space Physics, TIM Daily, https://lasp.colorado.edu/home/sorce/data/ accessed June 18, 2021.

[16] Clouds and Earth's Radiant System. 2021. CERES Input Data Sources, Total Solar Irradiance Information, https://ceres.larc.nasa.gov/data/general-product-info/#total-solar-irradiance-tsi-information and https://ceres.larc.nasa.gov/documents/TSIdata/CERES_EBAF_Ed2.8_DailyTSI.txt, accessed September 7, 2021.

[17] Bourassa, A. E., and A. Robock, W. J. Randel, T. Deshler, L. A. Rieger, N. D. Lloyd, E. J. T. Llewellyn, and D. A. Degenstein. 2012. Large volcanic aerosol load in the stratosphere linked to Asian monsoon transport, *Science* **337**, 78-81, http://dx.doi.org/10.1126/science.1219371.

[18] NASA Goddard Institute for Space Studies 2016. Forcings in GISS climate model, https://data.giss.nasa.gov/modelforce/strataer: GISS stratospheric aerosol optical depth at 550 nm, 2016. https://data.giss.nasa.gov/modelforce/strataer/tau.line_2012.12.txt, accessed December 8, 2021.

[19] Carn, S. A., P. A. Newman, V. Aquila, H. Gonnerman, and J. Dufek. 2021. Anticipating climate impacts of major volcanic eruptions, *Eos* **102**, August 31, https://doi.org/10.1029/2021EO162730.

[20] Kloss, C., G. Berthet, P. Sellitto, F. Ploeger, G. Taha, M. Tidiga , M. Eremenko, A. Bossolasco, F. Jégou, J.-B. Renard, and B. Legras, 2020, Stratospheric aerosol layer perturbation caused by the 2019 Raikoke and Ulawun eruptions and climate impact, *Atmospheric Chemistry and Physics Discussions*, 7 August 2020, https://doi.org/10.5194/acp-21-535-2021.

[21] Wolter, K., and M. S. Timlin, 2011. El Niño Southern Oscillation behaviour since 1871 as diagnosed in an extended multivariate ENSO index (MEI.ext), *International Journal of Climatology* **31**, 1074–1087, https://doi.org/10.1002/joc.2336.

[22] National Oceanic and Atmospheric Administration Physical Sciences Laboratory. 2011. MEI.ext Index. May 10, https://psl.noaa.gov/enso/mei.ext/table.ext.html, accessed December 17, 2021.

[23] National Oceanic and Atmospheric Administration Physical Sciences Laboratory. 2021. MEI.v2 values, https://psl.noaa.gov/enso/mei, accessed December 17, 2021.

[24] McCracken, K., G. J. Beer, F. Steinhilber, and J. Abreu. 2013. A phenomenological study of the cosmic ray variations over the past 9400 Years, and their implications regarding solar activity and the solar dynamo, *Solar Physics* **286** (2) 286:609–627, doi:10.1007/s11207-013-0265-0. https://doi.org/10.1007/s11207-013-0265-0.